

Transport Measurements of Strongly-Correlated Electrons on Helium in a Classical Point-Contact Device

D.G. Rees,^{1,*} I. Kuroda,^{1,2} C.A. Marrache-Kikuchi,^{1,†} M. Höfer,³ P. Leiderer,³ and K. Kono^{1,2}

¹*Low Temperature Physics Laboratory, RIKEN, Wako 351-0198, Japan*

²*Department of Physics, Tokyo Institute of Technology, Tokyo 152-8551, Japan*

³*Faculty of Physics, University of Konstanz, 78457 Konstanz, Germany*

(Dated: June 15, 2018)

We present transport measurements of electrons on the surface of liquid helium in a microchannel device in which a constriction may be formed by a split-gate electrode. The surface electron current passing through the microchannel first decreases and is then completely suppressed as the split-gate voltage is swept negative. The current decreases in a steplike manner, due to changes in the number of electrons able to pass simultaneously through the constriction. We investigate the dependence of the electron transport on the AC driving voltage and the DC potentials applied to the sample electrodes, in order to understand the electrostatic potential profile of the constriction region. Our results are in good agreement with a finite element modeling analysis of the device. We demonstrate that the threshold of current flow depends not only on the applied potentials but also on the surface electron density. The detailed understanding of the characteristics of such a device is an important step in the development of mesoscopic experiments with surface electrons on liquid helium.

PACS numbers: 73.20.-r, 73.23.-b, 85.30.Hi, 45.50.Jf

I. INTRODUCTION

An electron close to the free surface of liquid helium is subjected to an attractive force due to a weak image charge formed in the liquid^{1,2}. In the presence of an applied electric field E_z , the potential in the direction perpendicular to the helium surface may be written as $V(z) = -\Lambda e^2/z + eE_z z$ where $\Lambda = (\varepsilon - 1)/4(\varepsilon + 1)$, ε is the dielectric constant of the liquid, e is the absolute value of the electronic charge and z is the distance from the helium surface. The electron is prevented from entering the liquid due to a ~ 1 eV potential barrier at the surface and so remains localized above the liquid. The potential $V(z)$ gives rise to a series of bound states for perpendicular motion³; in the ground state, the expectation value of z is ~ 11 nm. The lifetime of these bound states is predicted to be long, leading to the proposal that electrons on the surface of liquid helium may be good candidates for quantum bits⁴.

For a two-dimensional system of charges on a liquid helium surface, the electron surface density n_s may be varied over a wide range, up to a theoretical limit given by the hydrodynamic instability of the bulk liquid surface⁵⁻⁷ of $\sim 2.2 \times 10^9$ cm⁻². By varying temperature the scattering processes which determine the electron mobility in the plane parallel to the helium surface may be controlled. Below ~ 0.8 K the density of gas atoms above the liquid surface becomes effectively zero and scattering occurs only with excitations of the liquid surface, ripplons, leading to high mobilities⁸ in excess of 10^8 cm²/V.s. As the Coulomb interaction between electrons is essentially unscreened, and the electron separation is much larger than the thermal electron wavelength, SSE have been used to study classical effects in strongly-interacting electron systems, such as the transition from an electron liquid to a 2D Wigner solid as the temperature of the

electron system is decreased⁹.

Quasi-one dimensional SSE systems¹⁰ have been investigated using samples in which liquid helium was confined in grooves on a dielectric substrate¹¹. The width of the grooves was as low as $1.25 \mu\text{m}$. In such experiments, the temperature dependence of the electron mobility¹² was found to be in good agreement with that predicted by theoretical calculations where transitions between quantized energy levels for the lateral motion of the electrons were taken into account¹³. However, for such dielectric substrates the mobility was also dependent on substrate defects in regions where the helium film was thin.

Recent experiments have made use of microchannel devices fabricated by lithographic techniques in order to study the properties of SSE in confined geometries. A schematic representation of a set of such microchannels is shown in Fig. 1. Placed a distance h above the bulk surface of superfluid helium, the channel will fill by capillary action; the helium surface may then be charged. The radius of curvature R of the liquid is given by $R = \alpha/\rho gh + n_s^2 e^2 / 2\varepsilon\varepsilon_0$ where α and ρ are the surface tension coefficient and density of liquid ⁴He respectively, g is the acceleration due to gravity and ε_0 is the dielectric constant of vacuum¹⁴. The transport of electrons in such devices was first demonstrated for a channel of width $30 \mu\text{m}$ and depth $1 \mu\text{m}$ ¹⁵. The non-linear transport of the Wigner solid on helium surfaces in microchannels of width $8\text{-}20 \mu\text{m}$ was studied in three-terminal devices comprising of source, drain and gate electrodes submerged beneath the helium surface^{16,17}. The ultra-efficient transfer of a small number of electrons along parallel microchannels of width $10 \mu\text{m}$, again using a series of gate electrodes beneath the helium surface, has also been demonstrated¹⁸. In still more advanced devices, small ensembles of electrons, including a single electron, trapped in a microfabricated circular pool of radius 10

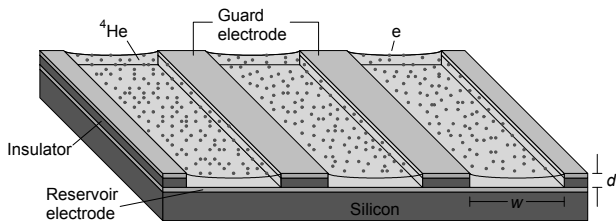


FIG. 1. Schematic picture of a set of microchannels. The microchannels are filled by the capillary action of superfluid ^4He , the surface of which is then charged with electrons.

μm , have been studied using a charge-sensitive superconducting Single Electron Transistor (SET) positioned beneath the helium surface¹⁹. A Field Effect Transistor (FET) for electrons on a thin helium film, where the electron density may exceed the hydrodynamic limit, has also been demonstrated²⁰. There the separation between the split-gate electrodes was $200\ \mu\text{m}$.

Such experiments demonstrate a progression towards the sensitive control and measurement of small numbers of SSE on helium, raising the possibility of studying novel phenomena associated with classically interacting charge systems in confined geometries. Many theoretical studies have been conducted on the behavior of such systems. In quasi-one dimensional systems, at sufficiently low temperatures, particles are predicted to form a series of rows, the number of which changes with the particle density or confinement strength, leading to structural phase transitions and re-entrant melting processes^{21,22}. Similar phenomena have also been predicted in circularly symmetric parabolic confinements²³. The pinning and depinning dynamics of charged particles at potential constrictions have also been investigated using Monte Carlo calculations^{24–26}. However, experimental difficulties have restricted progress towards investigating these phenomena. SET charge measurements, whilst extremely sensitive, may be plagued by intrinsic two-level fluctuator charge noise^{27,28}. Also, the electrostatic potential profile in microchannel devices may be distorted by contact potentials and surface charging effects which can be difficult to quantify²⁹.

As a step towards overcoming these experimental difficulties, we have performed transport measurements of SSE on superfluid ^4He in a microfabricated device. In this sample, two microchannel SSE reservoirs are separated by a split-gate electrode which, at appropriate bias, forms a constriction. As the split-gate voltage V_{gt} is swept negative the current I flowing through the constriction is reduced and then reaches zero at a threshold voltage V_{gt}^{th} . The appearance of step-like decreases in current in this device, where each step corresponds to a change in the number of electrons able to pass simultaneously through the constriction, has already been reported³⁰. Here we present further transport measurements, investigating in particular the response of the sys-

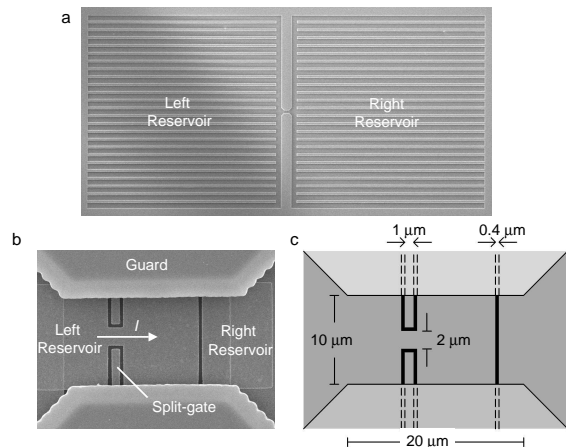


FIG. 2. Point-contact device for electrons on helium. (a) Two arrays of microchannels form the left and right electron reservoirs. (b) A split-gate electrode is positioned at the base of the small central channel which links the two reservoirs. (c) Diagram showing the dimensions of the electrodes in the central channel.

tem to increasing AC driving voltage, which causes significant non-linear transport effects to emerge. These results are discussed in relation to an electrostatic model of the sample which shows that offsets in electrode potentials, arising for reasons which are not yet clear, are important in determining the potential profile of the device.

II. EXPERIMENTAL

The sample used in this experiment was prepared using multilayer optical and electron-beam lithography on a Si wafer, the surface of which was oxidized. Two arrays of microchannels, defined by a guard electrode, act as electron reservoirs between which electrons may be exchanged. These left and right reservoirs consist of 25 microchannels of width $w = 20\ \mu\text{m}$ arranged in parallel and connected together at one end (Fig. 2(a)). The two reservoirs are separated by a smaller channel of width $10\ \mu\text{m}$ and length $20\ \mu\text{m}$. Electrodes were fabricated beneath the reservoir microchannels and are denoted as the left and right reservoir electrodes respectively. A split-gate electrode was fabricated at the base of the small central channel (Fig. 2(b)). The geometry of the central channel is shown in Fig. 2(c); the split gate was $1\ \mu\text{m}$ long and separated by a gap of $2.8\ \mu\text{m}$. The $400\ \text{nm}$ gap between left and right reservoir electrodes was placed $10\ \mu\text{m}$ to the right of the split gate in order to avoid the distortion of the potential profile of the constriction region. A $1.5\ \mu\text{m}$ thick layer of hard baked photoresist, which defined the microchannel depth d , separated the lower electrodes from the guard electrode. All metal layers were made of gold ($65\ \text{nm}$ thick) on top of a thin ($15\ \text{nm}$) titanium

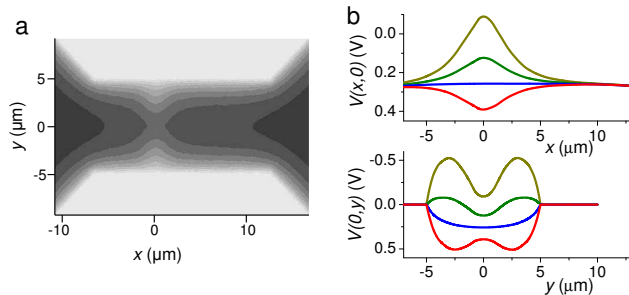


FIG. 3. (Color online) Finite element modeling results. (a) Contour plot of the calculated electrostatic potential in the central channel for $V_{gu} = V_{gt} = 0$ V and $V_r = +1.0$ V. The darker areas correspond to regions of lower potential energy for electrons. (b) Electrostatic potential in the x direction along the channel ($y = 0$ μm) and the y direction across the channel ($x = 0$ μm), for $V_{gu} = 0$ V, $V_r = 0.3$ V and $V_{gt} = +1.3$ V (red), $+0.3$ V (blue), -0.7 V (green), -2.3 V (dark yellow).

layer which was deposited in order to promote adhesion.

The sample was placed in an experimental cell approximately 0.5 mm above the bulk surface of superfluid ^4He at 1.25 K. The potentials V_{gu} , V_r and V_{gt} were applied to the guard, reservoir and split-gate electrodes, respectively. Under the bias conditions $V_{gu} = 0$ V, $V_r = V_{gt} = +1.0$ V, the surface of the helium was charged by thermionic emission from a small tungsten filament placed a few mm above the sample. A small AC voltage V_{in} of frequency 200 kHz was superimposed on the right reservoir electrode in order to drive electrons between the two reservoirs, through the central channel. The current I and conductance of the electron system G were determined by making a phase-sensitive measurement of the voltage capacitively induced on the left reservoir electrode, in reference to the standard lumped-circuit model³¹.

To aid the understanding of the electrostatic potential profile of the device, a finite element model of the central channel was developed³². The results of the modeling are shown in Fig. 3(a) for $V_{gu} = V_{gt} = 0$ V, $V_r = +0.3$ V. When V_{gt} is more negative than V_r , a saddle-point potential is formed on the helium surface at the point ($x = 0, y = 0$), with a maximum in potential for electrons in the x direction along the channel and a minimum in the lateral y direction. Fig. 3(b) shows how the potential profile develops as V_{gt} is changed. For $V_{gt} = -2.3$ V the potential at the center of the saddle-point is more negative than the guard electrode potential. We assume that the electrostatic potential energy of the electron system may not exceed V_{gu} , as this would lead to electrons escaping from the reservoirs, onto the thin helium film covering the guard electrode, through which they should rapidly drain away³³. Therefore, when the potential at the center of the saddle-point is more negative than the guard electrode potential, the resulting potential barrier between the two reservoirs should block electron trans-

port through the constriction.

III. RESULTS AND DISCUSSION

Before discussing experimental results, we first develop an electrostatic model of the device, following the approach presented previously³⁰. Note that in this model, a more positive voltage corresponds to a lower potential energy for an electron. We estimate that the change in the depth of the helium at the center of the 20 μm -wide reservoir microchannels should be less than 0.1 μm . Therefore we do not take the curvature of the helium surface into account here. We begin by assuming that the electron system may be considered as a charge continuum. The electrostatic potential energy of the electron system in the reservoirs, V_e , depends on the reservoir electrode voltage V_r and the electron density. Therefore we may write $V_e = -en_s d / \epsilon \epsilon_0 + V_r$. The results of the finite element modeling analysis (Fig. 3) indicate that a saddle-point potential is formed at the constriction between the two reservoirs when V_{gt} is more negative than V_r . At appropriate values of V_{gt} a potential barrier between the two reservoirs may be formed. The saddle-point potential may be written as $V(x, y) = V_b + \frac{1}{2}ax^2 - \frac{1}{2}by^2$ where V_b is the potential at the center of the saddle-point and a and b are constants. We consider that for $-eV_e > -eV_b$ electrons may pass over the potential barrier, allowing transport through the constriction, whereas for $-eV_e < -eV_b$ electron transport is blocked. The condition $-eV_e = -eV_b$ therefore defines the threshold of current flow through the constriction. This condition is depicted schematically in Fig. 4(a).

The influence of the reservoir, split-gate and guard electrodes on the potential barrier may be estimated by considering the region of space at the center of the constriction to have some capacitance to the three electrodes, C_r , C_{gt} and C_{gu} , as well as a stray capacitance to the surroundings C_s . The total capacitance of the region is then described by $C_\Sigma = C_r + C_{gt} + C_{gu} + C_s$ and we can define constants to represent the relative strength of coupling from each electrode to the barrier region as $\alpha = C_r / C_\Sigma$, $\beta = C_{gt} / C_\Sigma$, $\gamma = C_{gu} / C_\Sigma$ and $\sigma = C_s / C_\Sigma$. Experimentally it was found that, on increasing V_r , V_{gt} and V_{gu} by +100 mV simultaneously the threshold of current flow also increased by exactly +100 mV (data not shown), indicating that C_s was in fact negligibly small ($\sigma = 0$) and that $\alpha + \beta + \gamma = 1$. The potential at the center of the constriction may then be written as $V_b = \alpha V_r + \beta V_{gt} + \gamma V_{gu}$.

We now consider the case in which the reservoir voltage is set progressively more negative with a fixed bias applied to the split gate and guard electrode (here we assume V_{in} to be small). This is depicted schematically in Fig. 4(a-c); from top to bottom V_r goes from positive to negative bias. In Fig. 4(a) we see that, at a certain positive reservoir bias, the height of the potential barrier just meets the potential energy of the electron system and the current is ‘pinched-off’. Making V_r more negative (Fig.

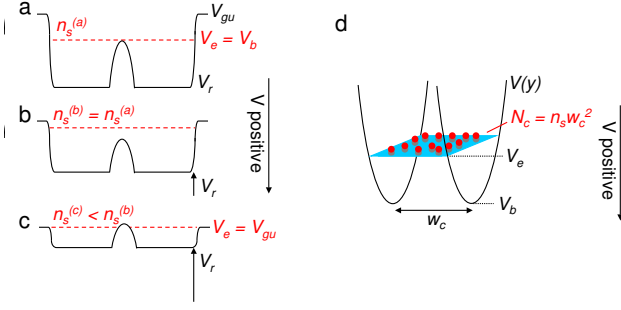


FIG. 4. (Color online) Two electrostatic models of the system. (a) Schematic diagram of the electrostatic potential across the device through the central channel, $V(x,0)$, for the case where $V_e = V_b$, assuming that the electron system forms a charge continuum. (b) As V_r becomes more negative, V_e becomes negative more quickly than V_b and V_{gt} must be set more negative to ‘pinch-off’ the current. (c) Eventually $V_e = V_{gu}$ and when V_r becomes more negative electrons are lost to the guard electrode. Because V_e now remains constant, V_{gt} must be set more positive to maintain the threshold condition. (d) Schematic representation of the constriction under a granular charge model in which the constriction is modeled as a small square of the helium surface of area $A = w_c^2$. The number of electrons in the constriction $N_c = n_s w_c^2$. Under this model, the current passing through the constriction should be suppressed when $N_c < 1$.

4(b)) causes both V_e and V_b to become more negative. As V_e remains below the guard potential electrons do not escape from the channels onto the thin helium film above the guard; there is no change in the electron density and V_e simply changes by the change in V_r . However, the change in the barrier height is smaller due its additional dependence on the split-gate and guard electrodes ($\alpha < 1$). Therefore a negative change in V_r causes V_b to become more positive relative to V_e and current flows across the barrier. By setting V_r more negative still (Fig. 4(c)) electrons are eventually lost to the guard leading to a reduction in n_s until V_e is equal to the guard potential. Now as V_r becomes more negative, V_b becomes more negative with respect to V_e and the current may eventually be suppressed once more.

We denote the value of V_{gt} for which $-eV_e = -eV_b$ as V_{gt}^0 . Following the model described above, expressions may now be derived to describe the dependence of V_{gt}^0 on V_r , for constant V_{gu} . From the threshold condition $-eV_e = -eV_b$, for the case where $-eV_e < -eV_{gu}$ we have

$$\frac{-en_s d}{\epsilon \epsilon_0} + V_r = \alpha V_r + \beta V_{gt}^0 + \gamma V_{gu} \quad , \quad (1)$$

and for the case where $-eV_e = -eV_{gu}$,

$$V_{gu} = \alpha V_r + \beta V_{gt}^0 + \gamma V_{gu} \quad . \quad (2)$$

Rearranging (1) and (2) gives respectively,

$$V_{gt}^0 = \frac{1-\alpha}{\beta} V_r - \frac{\frac{en_s d}{\epsilon \epsilon_0} + \gamma V_{gu}}{\beta} \quad , \quad (3)$$

and

$$V_{gt}^0 = \frac{-\alpha}{\beta} V_r + \frac{1-\gamma}{\beta} V_{gu} \quad . \quad (4)$$

Because the separation between the split-gate electrodes ($2.8 \mu\text{m}$) is comparable to the inter-electron spacing ($\sim 0.3 \mu\text{m}$ for $n_s = 1 \times 10^9 \text{ cm}^{-2}$), we expect only a small number of electrons to be in the constriction region when the system is close to the threshold condition. To estimate this number, we model the center of the constriction as a small square of area $A = w_c^2$, where w_c is the effective width of the constriction. As the FEM calculation indicates that the constant a is small compared to b , we will assume that the potential in the x direction is flat, whilst the electrons are confined in the y direction by a parabolic potential $V(y) = V_b - \frac{1}{2}by^2$, as pictured schematically in Fig. 4(d). The maximum lateral displacement for electrons in the constriction, y_{max} , satisfies the expression $V(y_{max}) = V_b - \frac{1}{2}by_{max}^2 = V_e$. Substituting $y_{max} = w_c/2$ gives

$$w_c = \sqrt{\frac{8}{b}(V_b - V_e)} \quad . \quad (5)$$

Note that for the threshold condition $-eV_e = -eV_b$, $w_c = 0$. Assuming a parallel-plate capacitor approximation, the charge density in the area A may be written as

$$n_c = \frac{\epsilon \epsilon_0}{ed}(V(y) - V_e) \quad , \quad (6)$$

and the total number of electrons in A is therefore

$$N_c = \frac{\epsilon \epsilon_0}{ed} \int_{-\frac{w_c}{2}}^{\frac{w_c}{2}} \int_{-\frac{w_c}{2}}^{\frac{w_c}{2}} (V(y) - V_e) dx dy \quad . \quad (7)$$

After integration over the limits as given by Eq. (5), we obtain the result

$$N_c = \frac{2}{3} \frac{8\epsilon \epsilon_0}{bed}(V_b - V_e)^2 \quad . \quad (8)$$

Although for the electron liquid electrons are not localized as in the Wigner crystal, we assume that electrons are distributed evenly over A , effectively forming a series of rows across the constriction. The number of electrons lying in the y direction across the constriction may then be estimated as $N_y = \sqrt{N_c}$. For constant V_r and V_{gu} , we also have the relation $V_b - V_e = \beta(V_{gt} - V_{gt}^0)$. This gives an expression relating N_y to V_{gt} as

$$N_y = \sqrt{\frac{2}{3} \frac{8\epsilon \epsilon_0}{bed} \beta (V_{gt} - V_{gt}^0)^2} \quad . \quad (9)$$

The number of electrons across the constriction should therefore increase linearly with increasing V_{gt} above the current threshold.

We suggest that the granularity of charge may cause some deviation from the behavior of the system as expected under the charge continuum model. From Eq.

(9), the value of V_{gt} for which one row of electrons may be formed in the constriction ($N_y = 1$) is

$$V_{gt}^1 = V_{gt}^0 + \frac{1}{\beta} \sqrt{\frac{3}{2} \frac{bed}{8\epsilon\epsilon_0}}. \quad (10)$$

For $V_{gt}^0 \leq V_{gt} < V_{gt}^1$ the number of electron rows across the constriction is less than 1. Therefore, as no electrons are present in the constriction, current flow should be suppressed when $V_{gt} = V_{gt}^1$ rather than at the threshold condition assumed under the charge continuum model $V_{gt} = V_{gt}^0$. We may now correct Eqs. (3) and (4) to give V_{gt}^1 for changing V_r at constant V_{gu} . For the case where $-eV_e < -eV_{gu}$ we have

$$V_{gt}^1 = \frac{1-\alpha}{\beta} V_r + \frac{1}{\beta} \sqrt{\frac{3}{2} \frac{b(V_r)ed}{8\epsilon\epsilon_0}} - \frac{\frac{en_s d}{\epsilon\epsilon_0} + \gamma V_{gu}}{\beta}, \quad (11)$$

and for the case where $-eV_e = -eV_{gu}$,

$$V_{gt}^1 = \frac{-\alpha}{\beta} V_r + \frac{1}{\beta} \sqrt{\frac{3}{2} \frac{b(V_r)ed}{8\epsilon\epsilon_0}} + \frac{1-\gamma}{\beta} V_{gu}. \quad (12)$$

Note that the value of b , which describes the parabolic lateral confinement at the constriction, is dependent on the potential applied to the reservoir electrodes (assuming constant V_{gu}). The FEM calculation of the potential profile shows this dependency to be linear. The corrective terms therefore introduce a non-linear dependence of V_{gt}^1 on V_r . However, in the following discussion, we will assume that, for constant V_r , small changes in V_{gt} cause a negligibly small change in b .

We have performed measurements in order to determine whether the charge continuum model or the granular charge model best describes the dynamics of electrons in the device. We denote the experimentally determined value of the split-gate voltage for which the current is suppressed as V_{gt}^{th} . Figure 5(a) shows the dependence of the current I flowing through the central channel as V_{gt} is varied for different values of the driving voltage V_{in} . The current decreases as V_{gt} is swept negative and finally is completely suppressed at the threshold voltage V_{gt}^{th} , which for all cases is more negative than the reservoir voltage $V_r = +1$ V. The linear dependence of V_{gt}^{th} on V_{in} is shown in Fig. 5(b). The threshold for current flow occurs at more negative split-gate bias as the driving voltage is increased.

Measurements of SSE current flow over a potential barrier formed by a split-gate electrode in a similar device have already been reported³⁴. There, for values of V_{in} up to 100 mV_{pp}, it was shown that current flow across a potential barrier could be induced by increasing V_{in} until the potential energy of the electron system could overcome the barrier, allowing electrons to be transferred between the reservoirs. Here we observe the same behavior. The dependence of V_{gt}^{th} on V_{in} is discussed in more detail later in this section.

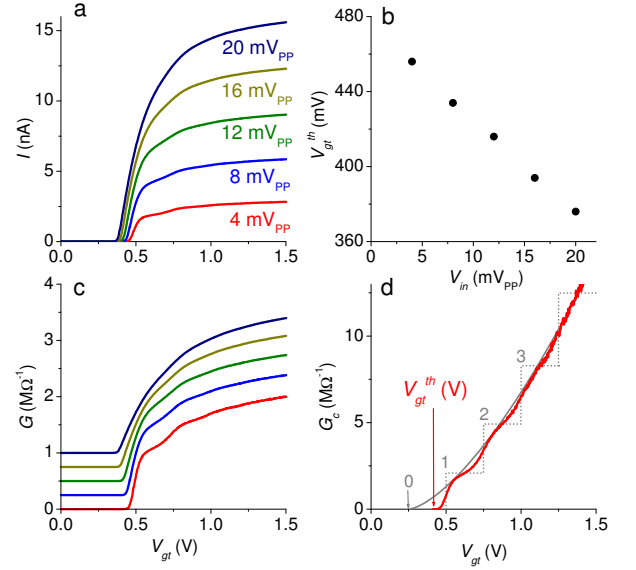


FIG. 5. (Color online) (a) Peak current I measured as a function of V_{gt} for different driving voltage amplitude V_{in} . (b) The current threshold V_{gt}^{th} against V_{in} . (c) Conductance of the electron system G as a function of V_{gt} for different V_{in} . Above 4 mV_{pp} each data set is shifted vertically for clarity. (d) Constriction conductance G_c for $V_{in} = 4$ mV_{pp}. G_c increases in a series of smoothed steps. The grey dotted line is a guide to the eye indicating values of V_{gt} at which, under the granular charge model, the number of electrons across the constriction increases by 1. The threshold V_{gt}^{th} lies between $N_y = 0$ and $N_y = 1$. The solid grey line is a guide to the eye of functional form $G_c \sim V_{gt}^{\frac{3}{2}}$ starting at $V_{gt} = 0.25$ V.

In Fig. 5(c) we show the corresponding conductance G for each current measurement. Above V_{gt}^{th} , G increases sharply for all values of V_{in} . Considering the saddle-point potential shown in the modeling results in Fig. 3, both the depth of the potential at the center of the constriction (which is proportional to the electron density in the constriction under the charge continuum model), and the effective width w_c of the constriction, should increase as V_{gt} is swept positive. Both effects should lead to an increase of conductance at the constriction. For high values of V_{gt} , where the split-gate electrode is more positive than the reservoir electrode and no potential barrier is expected to exist, G rises further, presumably due to the continuing increase of the electron density in the constriction region.

For still higher values of V_{gt} , the conductance eventually saturates. For $V_{in} = 4$ mV_{pp}, $G = 2.30$ MΩ⁻¹ at $V_{gt} = 3.0$ V. As the total conductance of the electron system no longer depends on the split-gate voltage in this region, we assume that the resistance of the constriction region is small compared to that of the electron system in the reservoirs. Therefore, the saturated conductance can be attributed to that of the reservoir region, and by subtracting the value of the resistance at

this split-gate voltage, $R = 1/G = 0.434 \text{ M}\Omega$, from the values of the resistance over the entire split-gate sweep, an approximation of the constriction resistance R_c can be calculated. The corresponding conductance of the constriction, $G_c = 1/R_c$, is shown in Fig. 5(d), for $V_{in} = 4 \text{ mV}_{pp}$. We see that above the conductance threshold, G_c increases in a series of steps. The steps are not a series of sharp rises and flat plateaus; rather, they appear smoothed-out. We add to the plot a guide to the eye (grey dotted line) indicating the manner in which a sharp step pattern fits the data. We align each sharp step with the maximum in the gradient at each increase in G_c . The spacing between the steps is $\Delta V_{gt} = 250 \text{ mV}$.

We suggest that the increasing number of electron rows across the constriction could lead to steplike increases in the constriction conductance. Such behavior is observed in other classical many-body systems with long-range interactions, such as pedestrians moving through bottlenecks³⁵. Here, such an effect is essentially the result of Coulomb blockade at a single constriction; for the case in which $N_y = 1$ and one electron row occupies the constriction, Coulomb repulsion prevents other electrons from passing through and electrons may only pass through in a single row. As the constriction is opened to the point where $N_y = 2$, the additional conduction channel should cause an increase in the constriction conductance as electrons may now pass freely through the constriction, side-by-side. The steplike increase in conductance resembles the quantized conductance steps observed in quantum point contact devices³⁶. From the FEM calculation results shown in Fig. 3(b), we estimate that the spacing of the energy subbands for lateral motion at the constriction to be $\sim 0.1 \text{ meV}$, which, as shown below, is much smaller than the change in V_b associated with each conductance step, and is also smaller than V_{in} . We therefore conclude that the origin of the steps observed here, due to the Coulomb interaction between electrons at the constriction, is quite different to the case of the quantum point contact, of which our device acts as a classical analogue.

The smoothing of the steps in G_c indicates that neither the charge continuum model, nor the granular charge model, describes the system precisely. We assume that the sharp steps fitted to the data in Fig. 5(d) correspond to the values of V_{gt} where, under the granular charge model, the number of electrons able to pass simultaneously through the constriction increases by 1. By extrapolation of these fitted steps, we can obtain an estimate of $V_{gt}^0 = 0.25 \text{ V}$. As described above, the constriction conductance should increase with increasing w_c and as V_b becomes more positive. The FEM calculation shows that $w_c \sim \sqrt{V_{gt}}$ whereas $V_b \sim V_{gt}$. We therefore naively expect the conductance of the constriction to vary as $G_c \sim V_{gt}^{\frac{3}{2}}$, under the charge continuum model. In Fig. 5(d) we plot the function $G_c = 1.04 \times 10^7 (V_{gt} - V_{gt}^0)^{\frac{3}{2}}$ (solid grey line). We see that this function describes G_c reasonably well, other than at points along the curve where the conductance is suppressed, which we attribute

to deviations from the continuum model due to the granular nature of charge. The agreement becomes closer for higher values of V_{gt} as the step features are lost, presumably as the number of electron rows increases and the electron system at the constriction better approximates a 2D charge continuum. We therefore conclude that whilst the granularity of charge causes observable deviations from the charge continuum model, and causes the current to be suppressed above the expected threshold V_{gt}^0 , the simplified approach depicted in Fig. 4(d) does not describe the system accurately. Correspondingly, the experimentally observed threshold of current flow, $V_{gt}^{th} = 0.456 \text{ V}$, lies between the values which we have estimated correspond to V_{gt}^0 and V_{gt}^1 .

We suggest that our experimental observation of the step-like increase in the conductance of the constriction may be verified by molecular dynamics simulations of classical charge systems at potential bottlenecks²⁴. Indeed, recent simulations of a system very similar to ours reproduce the smooth steplike increase in G_c , and show that each step is related to an increase in the number of electron rows across the constriction³⁷. These simulations also indicate that temporal fluctuations in the potential of electrons at the constriction, which are of thermal origin but essentially due to electron-electron interactions, and are not considered in our mean-field approach, cause the smoothing of the conductance steps. These fluctuations also cause V_{gt}^{th} to lie at values of V_{gt} more negative than V_{gt}^1 as, even for the case $N_y < 1$, there still exists some probability that the potential of electrons may be raised in order to overcome the barrier at the constriction, thus allowing transport. For our experiments, the driving voltage V_{in} causes an additional modulation of the electron density at the constriction over each AC cycle. In Fig. 5(c) the smoothing of the step-like features increases with increasing V_{in} , as discussed in more detail later in this section. However, we note here that extrapolation of the data shown in Fig. 5(b) to the limit $V_{in} = 0 \text{ mV}_{pp}$ yields a value of $V_{gt}^{th} \approx 0.47 \text{ V}$, which is a small change from the value recorded for $V_{in} = 4 \text{ mV}_{pp}$ and is still more negative than the value of $V_{gt}^1 = 0.5 \text{ V}$. Further comparison of our experimental results with numerical simulations is required to fully understand the dynamics of the electron system close to the conductance threshold.

We consider that the modulation of the potential of the electron system due to the applied driving voltage may cause additional non-linear behavior to appear in the electron transport properties close to the current threshold. To investigate such effects, the magnitude of the second harmonic component of the AC voltage induced on the left reservoir electrode, R_{2f} , was measured. In the case that the SSE AC current flow is perfectly sinusoidal in response to the driving voltage, the second harmonic component is zero. However, if the conductance should vary over each AC cycle, the current signal should become distorted causing higher frequency components to appear. In Fig. 6(a) we see that R_{2f} indeed rises as V_{gt}

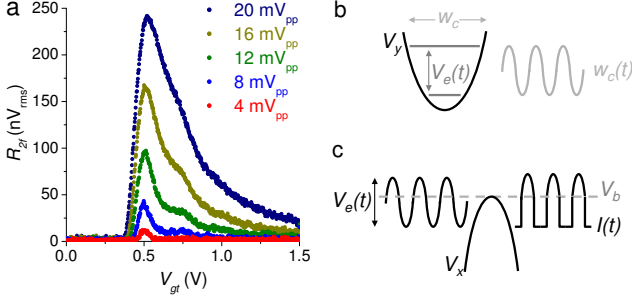


FIG. 6. (Color online) (a) Magnitude of the second harmonic component of the voltage signal, R_{2f} , as a function of V_{gt} for different driving voltages. (b) Processes giving rise to distortion in the AC current through a saddle-point potential. As the potential across the constriction V_y is parabolic, the effective width of the constriction w_c oscillates over each AC cycle of V_{in} , causing the conductance of the constriction region to vary over each cycle. (c) Close to the threshold of current flow, electrons may only pass intermittently across the potential barrier formed at the constriction.

is swept negative and reaches a maximum close to V_{gt}^{th} . The magnitude of R_{2f} increases with the driving voltage V_{in} .

In Fig. 6(b) and (c) we depict schematically two processes which may give rise to the distortion of the electron current through a saddle-point potential as the electron energy V_e is modulated. In the first case (Fig. 6(b)), when V_e is close to the bottom of the parabolic potential V_y , the effective width of the conductive channel w_c changes over the AC cycle which should lead to a time dependence of the conductance G . In addition, the effective depth of the potential for electrons at the constriction also varies, which should lead to a variation of the electron density, and so conductance, over each cycle. In the second case (Fig. 6(c)), as the potential maximum in V_x is raised and becomes higher than $V_e - V_{in}/2$, electrons are expected to flow only intermittently across the barrier.

In both of these cases, the degree of distortion in the current should reach a maximum close to the threshold of current flow. We therefore find the observed increase in R_{2f} close to the current threshold to be consistent with transport through a saddle-point potential. We also note that R_{2f} appears to rise in a series of weak peaks or steps which appear to mirror the step-like decrease in conductance observed in Fig. 5(c). We again find this to be consistent with our model. For values of V_{gt} where dI/dV_{gt} is large, modulating V_e gives rise to a large change in conductance over each AC cycle, and so the value of R_{2f} should be large. Each step in conductance should therefore be accompanied by a peak in R_{2f} . Indeed, the step-like feature in the conductance at $V_{gt} = 0.75$ V (Fig. 5(c)) is accompanied by a weak second peak in R_{2f} at the same split-gate voltage. However, the non-linear response of the SSE system to a driving field has been predicted by Saitoh³⁸ and observed experimentally³⁹. We

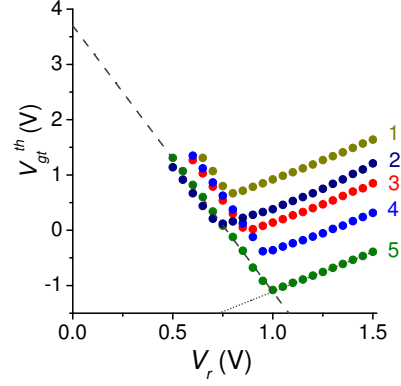


FIG. 7. (Color online) Measured values of V_{gt}^{th} for different values of V_r , which was varied from positive to negative values, and $V_{in} = 8$ mV_{pp}. The measurement was performed five times, as indicated by the different colors. The helium surface was charged at the start of each measurement. The dotted and dashed lines correspond to Eqs. (3) and (4) respectively. As explained in the text, for the data sets 1-5, $n_s = 0.70, 0.50, 0.99, 1.28, 1.48 \times 10^9$ cm⁻² respectively.

therefore note that the distortion in the current signal may also be due in some part to the intrinsic non-linear transport properties of the SSE system rather than solely due to the geometry or potential profile of the device.

The dependence of V_{gt}^{th} on V_r was investigated by measuring the current threshold for decreasing values of V_r , from 1.5 V to 0 V in 50 mV steps, for $V_{in} = 8$ mV_{pp}. The results of 5 such measurements, taken on different days, are shown in Fig. 7. In all 5 cases the split-gate voltage required to suppress the current initially becomes more negative as the reservoir potential is made more negative. Then, at a certain reservoir potential, the trend is reversed; the threshold moves to more positive values as the reservoir potential becomes more negative. In both cases the relationship between V_{gt}^{th} and V_r is approximately linear. These results are found to be in agreement with the behavior predicted by our electrostatic analysis. Starting at highly positive reservoir electrode bias, V_{gt} must initially be made more negative to suppress the current flow each time V_r is set more negative, to compensate for the reduction in the barrier height relative to V_e . Then, as electrons are lost to the guard, n_s decreases and V_e remains constant, the split-gate voltage must be made more positive to allow current flow with each step in V_r , due to the relative increase of the barrier height. The intersection between the two linear regions in the data marks the point at which electrons begin to escape to the guard. This point is different for each data set indicating that the initial surface density in each case was different. The intersection was not observed to occur for values of V_r greater than +1.0 V, the voltage at which the electron reservoirs were charged.

By making linear fits to the data presented in Fig. 7, we may derive values for α , β and γ based on the charge continuum model, using Eqs. (3) and (4), and

the relation $\alpha + \beta + \gamma = 1$. The values of the coupling constants were determined for each of the data sets. The similarity in the gradient of each data set indicates the stability of the coupling constants, the average values of which are shown in Table I.

We may also estimate α , β and γ taking into account the fact that the experimentally determined current threshold does not correspond exactly to V_{gt}^0 . The results in Fig. 5 show that V_{gt}^{th} appears to lie closer to V_{gt}^1 , the threshold under the granular charge model, as given by Eqs. (11) and (12). Whilst the constant b , which determines the deviation of V_{gt}^0 from V_{gt}^1 , may be estimated from the FEM modeling of the device, here we adopt a more straight-forward approach to take into account the deviation of V_{gt}^{th} from V_{gt}^0 . From Fig. 5, for $V_r = 1.0$ V, $V_{gt}^{th} - V_{gt}^0 = 0.16$ V. As discussed in more detail below, the reservoir electrode potential is equal to the guard electrode potential for $V_{gu} \approx 0.5$ V, due to an offset in the potential of the guard electrode. Because no parabolic confinement exists when $V_r = V_{gu}$, for this condition we expect $b = 0$ and therefore $V_{gt}^{th} - V_{gt}^0 = 0$ V. As the correction to V_{gt}^0 should display a square-root dependence on V_r , the value of V_{gt}^0 can be estimated for each value of V_r using the expression

$$V_{gt}^0 = V_{gt}^{th} - 0.16 \sqrt{\frac{V_r - 0.5}{1 - 0.5}}. \quad (13)$$

The average values for α , β and γ calculated using the values for V_{gt}^0 given by Eq. (13) are also listed in Table I.

The coupling constant β may also be estimated from dependence of V_{gt}^{th} on V_{in} shown in Fig. 5(b). We assume that, on increasing V_{in} , the increase in the barrier height required to suppress the current is equal to the corresponding increase in the maximum energy of the electron system in the right reservoir, $V_{in}/2$. Because, for fixed bias on the reservoir and guard electrodes, $\Delta V_b = \beta \Delta V_{gt}$ we may derive β from the gradient in Fig. 5(b) as $dV_{gt}^{th}/dV_{in} = -1/2\beta$. Similar measurements were made by sweeping the reservoir and guard potentials (data not shown) in order to determine the dependence of the thresholds V_r^{th} and V_{gu}^{th} on V_{in} . Under the charge continuum model, the constants α and γ may be given by $dV_r^{th}/dV_{in} = 1/2(1 - \alpha)$ and $dV_{gu}^{th}/dV_{in} = -1/2\gamma$. The results of these measurements (denoted dV^{th}/dV_{in}) are shown in Table I as well as the corresponding values calculated from the finite element model.

From the results shown in Table I, we see that, compared to the values calculated using Eqs. (3), (4), the change in α , β and γ when including the correction given by Eq. (13) is small. These values are also close to those given by measuring the dependence of V^{th} on V_{in} . All the experimentally determined values are in relatively good agreement with the FEM calculation. For all four results, α is largest and so the reservoir electrode dominates in determining the height of the potential barrier. This confirms that in our experiment, close to the conductance

threshold, the electrons are indeed passing through the region between the split-gate electrodes and above the reservoir electrode.

The determination of the constant β allows the expected change in V_{gt} to add one electron row across the constriction to be calculated using Eq. (10). We use the FEM model to obtain an estimate of $b = 2.5 \times 10^{11}$ Vm⁻² for $V_r = 1.0$ V and $V_{gu} = 0.62$ V. Using $\beta = 0.16$ we find that $V_{gt}^1 - V_{gt}^0 = 224$ mV. This value is in good agreement with the experimentally observed step separation, $\Delta V_{gt} = 250$ mV for $V_r = 1.0$ V (Fig. 5(d)), indicating that the step-like increases in G_c are indeed due to increases in the number of electrons across the constriction. The change in split-gate voltage ΔV_{gt} is related to the corresponding change in V_b by the constant β . For $\beta = 0.16$, $\Delta V_b \approx 40$ mV, which is comparable to V_{in} . We therefore conclude that the increase of smoothing of the steplike features with increasing V_{in} may be due to the modulation of the electron density at the constriction, which causes transport features arising from the discreet number of electrons across the constriction to be lost.

The data shown in Fig. 7 was taken with a voltage of 0 V applied to the guard electrode. From Eq. (4) it is then to be expected that $V_{gt}^{th} = 0$ V for $V_r = 0$ V. However, the intercept on the V_{gt}^{th} axis for each data set is typically +3.6 V indicating a true value of the guard potential of $V_{gu} \approx +0.62$ V. This apparent offset is confirmed experimentally for each of the data sets; below a value of $V_r \approx 0.5$ V the electron signal was lost completely indicating that at this point $V_r \approx V_{gu}$. The offset is seen to vary over a small range; for data sets with a higher intercept on the V_{gt}^{th} axis the electrons were lost at more positive values of V_r . Despite thermally cycling the device to room temperature and making efforts to ensure correct grounding of the experimental wiring the offset remained. However, the stability of the offset over many hours or days allowed consistent measurements to be made. Voltage offsets in mesoscopic devices may be caused by contact potential differences, thermoelectric effects or surface charging effects²⁹. The cause of the offset observed in this experiment is not yet clear. Taking the offset into account, the estimated initial surface electron densities for the data sets 1-5 shown in Fig. 7 are 0.70, 0.50, 0.99, 1.28, 1.48×10^9 cm⁻² respectively.

The melting temperature of the 2D Wigner solid depends on the electron density as $T_m = 0.225 \times 10^6 \sqrt{n_s}$ ¹⁶. For the case of a potential offset on the guard potential of +0.62 V, the saturated electron density achieved when charging the reservoirs with $V_r = +1$ V is $n_s = 1.48 \times 10^9$ cm⁻² which gives a value of $T_m = 0.866$ K. In Fig. 8 we show the temperature dependence of the resistance R of the electron system for $V_r = V_{gt} = +1.0$ V. At 1.23 K the current threshold was measured (inset). In reference to Fig. 7, the highly negative value of the threshold $V_{gt}^{th} = -0.29$ V indicates that the density was close to saturation. The increase in R below 1 K is attributed to the formation of the 2D Wigner solid. The localization of electrons in the Wigner lattice leads to the formation

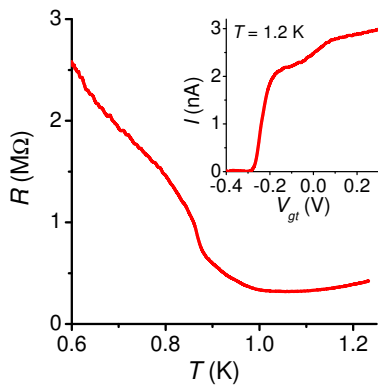


FIG. 8. (Color online) Resistance against temperature for the case in which the constriction is widely opened ($V_{gt} = +1$ V) for $V_{in} = 5$ mV_{pp}. Inset: I as a function of V_{gt} for the same electron density, measured at 1.23 K.

of a small depression, or dimple, in the helium surface beneath each electron, which increases the electron effective mass, and so resistivity of the system⁴⁰. Recent experiments have investigated the transport of the Wigner solid in a microchannel geometry where the decoupling of the electron lattice from the dimple lattice at high driving fields leads to a highly non-linear response¹⁷. In our measurement, a sharp increase in the resistance is observed at $T \approx 0.875$ K which may correspond to the melting temperature of the electron system, in agreement with the predicted value of T_m for the case in which the guard potential is offset.

IV. CONCLUSIONS

We have investigated the AC transport of strongly-correlated electrons on the surface of liquid helium at a

constriction formed by a split-gate electrode. The electron current may be suppressed by sweeping the voltage of the split gate negative. The threshold for current flow was dependent on the DC voltages of all the device electrodes and the AC driving voltage applied to the electron system, as well as the electron density. Step-like increases in the conductance of the electron system as the split-gate voltage was swept positive were found to be due to increases in the number of electrons able to pass simultaneously through the constriction. The device therefore acts as a classical analogue of the quantum point contact. Our results are in good agreement with a simple model of the device developed with the aid of finite element analysis software in which a saddle-point potential profile is formed at the constriction. Comparison with this model reveals that a potential offset on the guard electrode of the device plays a crucial role in determining the potential profile of the sample. Such detailed characterization of microfabricated samples for electrons on the surface of liquid helium is an important step towards the realization of more advanced mesoscopic devices such as single electron devices and quasi-one dimensional wires.

ACKNOWLEDGMENTS

We thank M. Dykman, F. Nori, K. Ono, H. Totsuji, M. Araki and H. Hayakawa for useful discussions. This work was partially supported by Kakenhi. DGR was supported by the RIKEN FPR program.

-
- * drees@riken.jp
 † Present address: CSNSM, Bat. 108, 91405 Orsay, France
¹ E. Andrei (ed.), *Two-dimensional electron systems on helium and other cryogenic substrates*. (Kluwer Academic, Dordrecht, 1997)
² Y.P. Monarkha, K. Kono, *Two-Dimensional Coulomb Liquids and Solids* (Springer-Verlag, Berlin, 2004)
³ C.C. Grimes, et al., Phys. Rev. B **13**(1), 140 (1976)
⁴ P.M. Platzman, M.I. Dykman, Science **284**, 1967 (1999)
⁵ L. Gor'kov, D. Chernikova, JETP Lett. **18**(2), 68 (1973)
⁶ P. Leiderer, M. Wanner, Phys. Lett. A **73**(3), 189 (1979)
⁷ M. Wanner, P. Leiderer, Phys. Rev. Lett. **42**(5), 315 (1979)
⁸ K. Shirahama, S. Ito, H. Suto, K. Kono, J. Low Temp. Phys. **101**, 439 (1995)
⁹ C.C. Grimes, G. Adams, Phys. Rev. Lett. **42**(12), 795 (1979)
¹⁰ Y.Z. Kovdria, Low Temp. Phys. **29**(77) (2003)

- ¹¹ Y.Z. Kovdria, V.A. Nikolaenko, Sov. J. Low Temp. Phys. **18**(894) (1992)
¹² Y.Z. Kovdria, et al., J. Low Temp. Phys. **110**(1), 191 (1998)
¹³ S.S. Sokolov, G.Q. Hai, N. Studart, Phys. Rev. B **51**(9), 5977 (1995)
¹⁴ D. Marty, Journal of Physics C: Solid State Physics **19**(30), 6097 (1986)
¹⁵ R. van Haren, et al., Physica B: Condensed Matter **249-251**, 656 (1998)
¹⁶ P. Glasson, et al., Phys. Rev. Lett. **87**(17), 176802 (2001)
¹⁷ H. Ikegami, H. Akimoto, K. Kono, Phys. Rev. Lett. **102**(4), 046807 (2009)
¹⁸ G. Sabouret, et al., Appl. Phys. Lett. **92**(8), 082104 (2008)
¹⁹ G. Papageorgiou, et al., Appl. Phys. Lett. **86**(15) (2005)
²⁰ J. Klier, I. Doicescu, P. Leiderer, J. Low Temp. Phys. **121**(5-6), 603 (2000)
²¹ A.V. Chaplik, Pis'ma Zh. Eksp. Teor. Fiz. **31**, 275 (1980)

- ²² G. Piacente, I.V. Schweigert, J.J. Betouras, F.M. Peeters, Phys. Rev. B **69**(4) (2004)
- ²³ V.M. Bedanov, F.M. Peeters, Phys. Rev. B **49**(4), 2667 (1994)
- ²⁴ G. Piacente, F.M. Peeters, Phys. Rev. B **72**(20), 205208 (2005)
- ²⁵ C.J. da Silva, J.P. Rino, L. Cândido, Phys. Rev. B **77**(16), 165407 (2008)
- ²⁶ P. Damasceno, C. DaSilva, J. Rino, L. Cndido, J. Low Temp. Phys. **160**, 58 (2010)
- ²⁷ N.M. Zimmerman, J.L. Cobb, A.F. Clark, Phys. Rev. B **56**(12), 7675 (1997)
- ²⁸ D.G. Rees, et al., Appl. Phys. Lett. **93**(17), 173508 (2008)
- ²⁹ E. Rousseau, et al., Phys. Rev. B **79**(4), 045406 (2009)
- ³⁰ D.G. Rees, et al., Phys. Rev. Lett. **106**(2), 026803 (2011)
- ³¹ Y. Iye, J. Low Temp. Phys. **40**(5-6), 441 (1980)
- ³² The FEM modeling was performed using FlexPDE software, PDE Solutions Inc.
- ³³ J. Angrik, A. Faustein, J. Klier, P. Leiderer, J. Low Temp. Phys. **137**, 335 (2004)
- ³⁴ D.G. Rees, K. Kono, J. Low Temp. Phys. **158**(1-2), 301 (2010)
- ³⁵ S.P. Hoogendoorn, W. Daamen, Transportation Science **39**(2), 147 (2005)
- ³⁶ B.J. van Wees, et al., Phys. Rev. Lett. **60**(9), 848 (1988)
- ³⁷ M. Araki, H. Hayakawa, ArXiv e-prints (arXiv:1104.4854) (2011)
- ³⁸ M. Saitoh, T. Aoki, Journal of the Physical Society of Japan **44**(1), 71 (1978)
- ³⁹ F. Bridges, J.F. McGill, Phys. Rev. B **15**(3), 1324 (1977)
- ⁴⁰ Y.P. Monarkha, V.B. Shikin, Sov. Phys. JETP **41**, 710 (1975)

TABLE I. Coupling constants α, β and γ as calculated by the finite element analysis and the values measured experimentally from the results shown in Fig. 5 and Fig. 7.

Coupling constant	Calculated (FEM)	Measured (Eqs. (3), (4))	Measured (Eq. (13))	Measured (dV^{th}/dV_{in})
α	0.75	0.77	0.79	0.83
β	0.10	0.16	0.15	0.10
γ	0.15	0.07	0.06	0.07